Atmos. Chem. Phys., 24, 12409–12423, 2024
https://doi.org/10.5194/acp-24-12409-2024

Atmospheric Chemistry and Physics
Open Access
EGU

Rapid oxidation of phenolic compounds by O_3 and $HO^{\cdot}$: effects of the air–water interface and mineral dust in tropospheric chemical processes

Yanru Huo[1,2], Mingxue Li[3], Xueyu Wang[4], Jianfei Sun[5], Yuxin Zhou[1], Yuhui Ma[1], and Maoxia He[1]

[1]Environment Research Institute, Shandong University, Qingdao 266237, PR China
[2]Department of Atmospheric and Oceanic Sciences, McGill University, 805 Sherbrooke Street West, Montréal, QC H3A 0B9, Canada
[3]Department of Civil and Environmental Engineering, The Hong Kong Polytechnic University, Hong Kong SAR, PR China
[4]College of Geography and Environmental Sciences, Zhejiang Normal University, Jinhua 321004, PR China
[5]School of Environmental and Materials Engineering, Yantai University, Yantai 264005, PR China

Correspondence: Maoxia He (hemaox@sdu.edu.cn)

Received: 30 November 2023 – Discussion started: 6 February 2024
Revised: 14 September 2024 – Accepted: 19 September 2024 – Published: 11 November 2024

Abstract. Environmental media affect the atmospheric oxidation processes of phenolic compounds (PhCs) released from biomass burning in the troposphere. To address the gaps in experimental research, phenol (Ph), 4-hydroxybenzaldehyde (4-HBA), and vanillin (VL) are chosen as model compounds to investigate their reaction mechanism and kinetics at the air–water (A–W) interface, on TiO_2 mineral aerosols, in the gas phase, and in bulk water using a combination of molecular dynamics simulation and quantum chemical calculations. Of the compounds, Ph was the most reactive one. The occurrence percentages of Ph, 4-HBA, and VL staying at the A–W interface are $\sim 72\,\%$, $\sim 68\,\%$, and $\sim 73\,\%$, respectively. As the size of $(TiO_2)_n$ clusters increases, the adsorption capacity decreases until $n > 4$, and beyond this, the capacity remains stable. A–W interface and TiO_2 clusters facilitate Ph and VL reactions initiated by the O_3 and $HO^{\bullet}$, respectively. However, oxidation reactions of 4-HBA are little affected by environmental media because of its electron-withdrawing group. The O_3- and $HO^{\bullet}$-initiated reaction rate constant (k) values follow the order of $A\text{–}W_{Ph} > TiO_{2\,VL} > A\text{–}W_{VL} > A\text{–}W_{4\text{-}HBA} > TiO_{2\,4\text{-}HBA} > TiO_{2\,Ph}$ and $TiO_{2\,VL} > A\text{–}W_{Ph} > A\text{–}W_{VL} > TiO_{2\,4\text{-}HBA} > TiO_{2\,Ph} > A\text{–}W_{4\text{-}HBA}$, respectively. Some byproducts are more harmful than their parent compounds, so they should be given special attention. This work provides key evidence for the rapid oxidation observed in the $O_3/HO^{\bullet}$ + PhC experiments at the A–W interface. More importantly, differences in the oxidation of PhCs by different environmental media due to the impact of substituent groups were also identified.

1 Introduction

Biomass burning, stemming from natural wildfires and human activity, significantly contributes to atmospheric particulate matter (PM). Biomass burning is a primary source of approximately 90 % of the global primary organic aerosols (POAs) and releases a substantial quantity of organic pollutants (Ito and Penner, 2005; Chen et al., 2017, 2023). Biomass burning is to blame for about 62 % of the total annual emissions of about 8.0 Tg of black carbon and 93 % of the total annual emissions of about 33.9 Tg of organic carbon worldwide (Bond et al., 2004). Emissions from biomass combustion are one of the primary sources of atmospheric and particle pollutants that negatively affect human health, air quality, and climate (Reid et al., 2005; Yao et al., 2016). One of the three main types of biopolymers responsible for the formation of biomass is lignin (Sun et al., 2011), which is also the polymeric organic molecule most abundant in

plants (Lou et al., 2010; Soongprasit et al., 2020). Pyrolysis of lignin releases phenolic compounds (PhCs) into the air, including phenols, phenolic aldehydes, and methoxyphenols. By mass, these PhCs make up between 21 % and 45 % of the aerosol composition (Hawthorne et al., 1989; Diehl et al., 2013; Liao et al., 2020; Soongprasit et al., 2020). Methoxyphenols are one of the potential tracers that can be found in atmospheric wood smoke pollution, with the emission rate ranging from 900 to 4200 mg kg^{-1} fuel (Hawthorne et al., 1989; Rogge et al., 1998; Simoneit, 2002; Chen et al., 2017). Evidence shows that the oxidation processes of PhCs can result in the formation of secondary organic aerosol (SOA) (Yee et al., 2013; Jiang et al., 2023). Hence, it is imperative to explore the effects of PhCs when exposed to atmospheric oxidants.

After being released into the atmosphere, PhCs will be oxidized by ozone (O_3) and hydroxyl radicals ($HO^•$). Both are significant contributors to SOA (Arciva et al., 2022). The homogenous oxidation of PhCs has been the emphasis of previous studies (Henry et al., 2008; Yee et al., 2013; Liu et al., 2019; Arciva et al., 2022). In the past decade, researchers have investigated the kinetics and reaction mechanisms of gas-phase interactions of PhCs with O_3 and $HO^•$ (Kroflič et al., 2018; Smith et al., 2016; J. Sun et al., 2021; Y. Sun et al., 2021; Liu et al., 2022). Furthermore, they have investigated the hydroxylation, ring opening, and oligomerization processes of PhCs in the atmospheric liquid phase, with a focus on the potential environmental toxicity and climatic effects of these events (Ma et al., 2021; Liu et al., 2022; Arciva et al., 2022; Carena et al., 2023).

However, there is a dearth of specific data as well as of explanations of the mechanisms involved in the atmospheric oxidation of PhCs at the air–water (A–W) interface. The atmosphere contains a high concentration of aqueous aerosols and water microdroplets (Zhong et al., 2019; Guzman et al., 2022). The oxidation of PhCs can rapidly occur at the A–W interface (Rana and Guzman, 2022c). The term "water surface catalysis" denotes the phenomenon where chemical reactions happen at a faster rate at the A–W interface compared to the bulk phase (Lee et al., 2015a, b; Yan et al., 2016; Banerjee et al., 2017). In chemical engineering, titanium dioxide (TiO_2) is an essential photoactive component found in atmospheric mineral dust (Sakata et al., 2021; Wang et al., 2023). The interaction between PhCs and TiO_2 is continuous (Grassian, 2009; Rubasinghege et al., 2010; Shang et al., 2021), despite the relatively low prevalence of TiO_2 mineral particles (comprising 0.1 % to 10 % by mass). Therefore, it is essential to investigate the disparity between the oxidation reaction mechanisms and kinetics of PhCs at the A–W interface and mineral dust particles.

Increasing the number of constituents on the aromatic ring would affect the reactivity and lead to complex compounds after reaction addition and/or open-ring pathways. Phenol (Ph), 4-hydroxybenzaldehyde (4-HBA), and vanillin (VL) are typical lignin pyrolysis products (Jiang et al., 2010; Kibet et al., 2012). Thus, we selected Ph, 4-HBA, and VL as model compounds to present comprehensive mechanistic information at the A–W interface, on TiO_2 clusters, in the gas phase, and in bulk water, using a combination of molecular dynamics simulation and quantum chemical calculations. Rate constants were calculated within a wide temperature range in various environmental media. Additionally, computational toxicology was employed to evaluate the ecotoxicological impact of PhCs and their transformation products.

2 Methods

2.1 Molecular dynamics simulation

All of the molecular dynamics simulations were carried out by utilizing the GROMACS 2019 package, which included the AMBER force field. Parametrization of the Ph, 4-HBA, and VL was accomplished using the GAFF force field in conjunction with RESP charge calculations performed at the M06-2X/6-311++G(3df,2p)//M06-2X/6-31+G(d,p) level. The TIP3P water model was utilized so that individual water molecules may be represented (Jämbeck and Lyubartsev, 2014).

2.1.1 Properties of Ph, 4-HBA, and VL at the A–W interface

Considering the significance of the interfacial behavior of Ph, 4-HBA, and VL at the A–W interface, the properties of these three substances were initially examined by focusing on the A–W interface. Figure S1a in the Supplement depicts a rectangular box that has dimensions of $4 \times 4 \times 9\,nm^3$ and has a z axis that is perpendicular to the A–W contact. This box was used for all simulations. A water box that is too small may cause the central PhC molecules to be too close to the interface region, leading to inaccurate results. Conversely, opting for a water box that is too large can lead to an unnecessary waste of computational resources. To begin the process of constructing the initial configurations, a water slab measuring $4 \times 4 \times 4\,nm^3$ was positioned at the coordinates (2, 2, 4.5 nm) of the center of mass (COM). Because the rest extension along the z axis of the box was sufficiently large ($2.5\,nm^3$), it was possible to steer clear of the intersection of two A–W interfaces. Prior to the formal simulation, six Ph molecules were randomly selected and placed in a vacuum above the water box for 150 ns of NVT molecular dynamics simulation. The purpose of simulating 150 ns is to capture the fundamental molecular dynamics that occur on this timescale, such as bond formation, conformational changes, and interaction events. The results show no significant π–π interactions or formation of hydrogen bonds between the Ph molecules. To simplify the model, this was followed by simulations of individual molecules. Ph, 4-HBA, and VL were each placed in their own compartment at the coordinates (2.0, 2.0, 7.75 nm) for each system in order to simulate the behav-

ior of these molecules in the A–W interface region of cloud/fog drops and aerosol liquid water (ALW). To begin, the three different systems were optimized to use the least amount of energy possible. After that, NVT molecular dynamics simulations were carried out for a total of 150 ns.

2.1.2 Umbrella sampling simulations

In Fig. S1b, the molecule of Ph, 4-HBA, or VL was placed inside the box (their COM is (2.00, 2.00, 6.00 nm)), which is located directly 2.00 nm away from the COM of the water slab. The distance between the COM of Ph, 4-HBA, or VL and that of the water slab was used as the definition for the reaction coordinate (Fig. S1). The weighted histogram analysis approach, also known as WHAM, can be used to calculate the free-energy profiles of Ph, 4-HBA, or VL when they transition from the gas phase into bulk water (Kumar et al., 1992; Hub et al., 2010); details about WHAM are in Text S1 in the Supplement.

2.1.3 Radial distribution function

Estimating the strength of hydrogen bonds (HBs) between specific atoms can be done with the help of a tool known as the radial distribution function (RDF). Text S2 has an explanation of the characteristics of the RDF and the coordination number.

2.2 Density functional theory (DFT) calculations

In this work, all structural optimization and energy calculations were accomplished by utilizing the Gaussian 16 program (Frisch et al., 2016). Calculated at the CCSD(T)/cc-pVDZ, CBS-QB3, B3LYP/6-311+G(d,p), MP2/6-311+G(d,p), and M06-2X/6-311+G(d,p) levels, Cao et al. (2021) found that M06-2X/6-311++G(3df,2p)//M06-2X/6-31+G(d,p) is reliable for PhCs in the gas phase. After analyzing the stability of the wave function, the method we used is reliable. Therefore, all calculations for gas-phase reactions are performed at this level. Text S3 contains a description of the additional calculated details. The frequency correction factor (0.967) has been taken into account. Multiwfn (Lu and Chen, 2012) was used to construct the electron density map. This program integrates Visual Molecular Dynamics (version 1.9.3) (Humphrey et al., 1996) in order to conduct an analysis of the electrostatic potential (ESP) and the average local ionization energy (ALIE).

2.3 IRI analysis

Interaction region indicator (IRI) analysis (Lu and Chen, 2021) was used to determine the chemical bonds and weak interactions of Ph–4-HBA–VL adsorbed to TiO_2 clusters (the details are in Text S4).

2.4 Kinetic calculations

Text S5 contains an explanation of the kinetic calculation methods.

3 Results and discussion

3.1 Enrichment of Ph, 4-HBA, and VL at the A–W interface

3.1.1 The uptake of gaseous PhCs at the A–W interface

Figures S1 and S2 illustrate the relative distributions of water, O_3, and PhC molecules (Ph, 4-HBA, and VL) in the A–W interface system along the z axis. Hydroxyl radicals ($HO^•$) are primarily situated at the A–W interface contact, with the potential to diffuse through the water slab interior (Roeselová et al., 2004). Figure 1a displays the variation in water density along the z-coordinate distance from 0 to 9 nm, categorizing three zones: the A–W interface (2.25 to 2.79 and 6.21 to 6.75 nm), air (0 to 2.25 and 6.75 to 9 nm), and bulk water (2.79 to 6.21 nm). This method accurately determines the interfacial range (Zhang et al., 2019; Shi et al., 2020). According to location definitions, the O_3 percentage distribution was as follows: 26 % at the A–W interface, 72 % in the air, and 2 % in bulk water (Fig. 1b). Figure 1c depicts molecular dynamics (MD) trajectories of Ph diffusion through the water slab from the air region over a 150 ns period. Ph is distributed in the air (8 %) and bulk water (20 %), with the majority at the A–W interface (72 %) (Fig. 1d). The majority of 4-HBA and VL molecules are located at the A–W interface, constituting 68 % and 73 % of the total locations as presented in Fig. S2.

In Fig. 2a, we observe the three key processes involving PhCs (Ph, 4-HBA, or VL) diffusing into the water slab from the air region: (i) the mutual attraction of gaseous Ph, 4-HBA, or VL; (ii) the uptake of PhCs (Ph, 4-HBA, or VL) at the A–W interface; and (iii) the hydration reaction of PhCs (Ph, 4-HBA, or VL) in the bulk water. Figure 2b displays the free-energy profile of the trajectories as Ph, 4-HBA, and VL transition from the air into the bulk water (see Text S6 for calculations details). The $\Delta G_{\text{gas}\rightarrow\text{interface}}$ values are $-0.22\,\text{kcal mol}^{-1}$ for the Ph–A–W (phenol–air–water) system, $-0.45\,\text{kcal mol}^{-1}$ for the A–$W_{4\text{-HBA}}$ (4-hydroxybenzaldehyde at the air–water interface) system, and $-0.20\,\text{mol}^{-1}$ for the A–W_{VL} (vanillin–air–water) system. This finding is consistent with previous studies about per- and polyfluoroalkyl substances (PFASs) at the A–W interface (Yuan et al., 2023). These values suggest that it is thermodynamically favorable for PhCs to approach the interfacial water molecules. Figure S3 illustrates typical snapshots from the trajectories of PhCs (Ph, 4-HBA, or VL). Initially, one molecule of Ph, 4-HBA, or VL was placed in the center of the water box, with an equivalent COM distance of 2 nm between the PhCs and the air phase. Subsequently, the PhCs moved closer to the interface, leading to adsorption at the A–

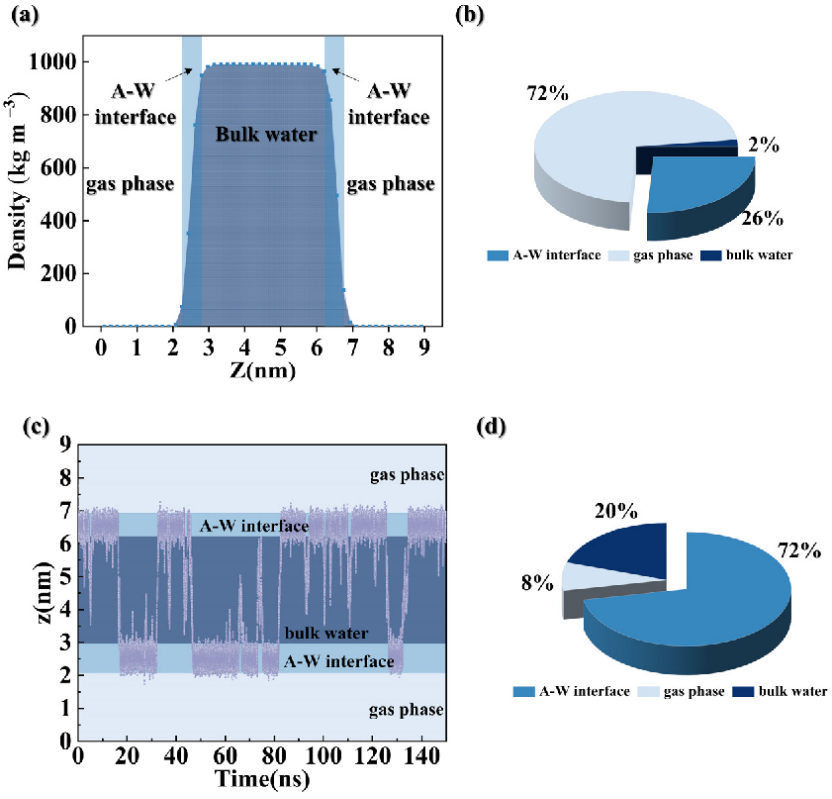

Figure 1. **(a)** Relative concentration distributions in the A–W system along the z axis; **(b)** probability of O_3 at the A–W interface, in gas phase, and in bulk water; **(c)** MD trajectories of Ph diffusion through the water slab over a 150 ns period; **(d)** probability of Ph at the A–W interface, in gas phase, and in bulk water.

W interface. During the adsorption process, the H atom of the phenolic hydroxyl group binds to the oxygen atom of the H_2O molecules at the A–W interface, forming H bonds and preventing its return to the bulk water. This property allowed the phenolic hydroxyl groups on PhCs to effectively adhere to the A–W interface, consistent with the experimental observations using steady-state interfacial vibrational spectra (Kusaka et al., 2021) and Fourier transform infrared (FTIR) imaging micro-spectroscopy (Guzman et al., 2022). Based on these findings, compared to the number of PhC molecules distributed in the gas phase and in bulk water, the location where air and water meet exhibits an increase in the number of PhC molecules.

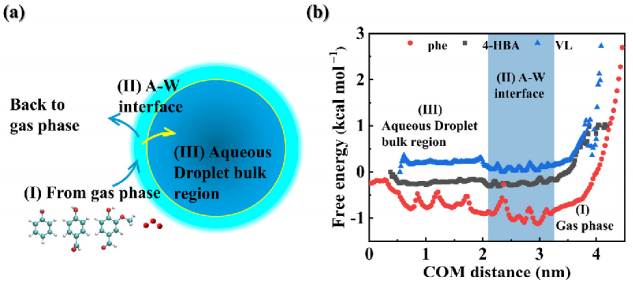

Figure 2. **(a)** Three key processes for the reaction of gaseous PhCs (Ph, 4-HBA, or VL) with the water drops; **(b)** free-energy change profile of gaseous PhCs (Ph, 4-HBA, or VL) approaching the bulk water.

3.1.2 Interface properties of PhCs

Introducing more hydrophilic functional groups increases the characteristic angle α and β of PhCs at the interface, allowing for more secure adsorption at the water–air interface. The interaction between H_{PhCs} and O_{H_2O} is the primary factor influencing the stability of PhCs at the interface. The coordination numbers (N) of $H_{Ph\text{-}OH}-O_{H_2O}$, $H_{4\text{-}HBA\text{-}OH}-O_{H_2O}$, and $H_{VL\text{-}OH}-O_{H_2O}$ are 2.68, 2.51, and 2.09, respectively. The number of functional groups attached to the benzene ring affects the N value; a higher number of functional groups leads to a lower N value. The reason for this is that aldehyde and methoxy are strong electron-withdrawing groups, which will reduce the conjugation effect between the benzene ring and the hydroxyl group and make the hydrogen atom on the hydroxyl group partially positively charged, thus weakening the hydrogen bonding ability with water molecules. See Text S7 for the interface properties of PhCs.

3.2 Adsorption of Ph, 4-HBA, and VL by TiO_2 clusters

The placement of PhCs on TiO_2 clusters significantly impacts adsorption energies (Bai et al., 2020). The adsorption capacity of pollutants on cluster surfaces is a key factor influencing degradation efficiency (Qu and Kroes, 2006). The primary mechanism of C atom adsorption to $(TiO_2)_n$ ($n = 1$–4) clusters occurs at a range of 2.57 to 2.61 Å and involves interaction between the H_{-OH} atom and the O_{TiO_2} atom, as seen in Fig. 3a. Hydrogen bonds can be formed between the H_{-OH} atom and the O_{TiO_2} atom (1.80–2.61 Å), improving the adsorption capacity. In contrast, Ph adsorption to $(TiO_2)_n$ ($n = 5$–6) clusters, ranging from 2.08 to 2.09 Å, is primarily due to interaction between the Ti atom and O_{-OH} atom. For a detailed description, see Text S8.

Adsorption energy a metric of adsorption capacity, is illustrated in Fig. 3b–d for Ph, 4-HBA, and VL on $(TiO_2)_n$ ($n = 1$–6). TiO_2 exhibits the highest adsorption capacity for Ph ($\Delta G_{ad} = -72.35\,kcal\,mol^{-1}$) (Fig. 3b). The adsorption energy values of TiO_2 and $(TiO_2)_3$ for 4-HBA and VL are -45.32 (Fig. 3c) and $-102.46\,kcal\,mol^{-1}$ (Fig. 3d), respectively. Physisorption energy ranges from -1.20 to $9.56\,kcal\,mol^{-1}$ (Nollet et al., 2003); thus the adsorption process in this study is spontaneous chemical adsorption. However, the capacity of TiO_2 to adsorb VL is significantly higher than that to adsorb Ph and 4-HBA. Figure 3b–d show that the adsorption capacity falls as the size of TiO_2 clusters increases when $n \leq 4$. In contrast, the adsorption capacity remains constant when $n > 4$. IRI measurements of Ph on the $(TiO_2)_n$ surface (Fig. 3e) reveal Ph–TiO_2 hydrogen bonds (H_{Ph}–O_{TiO_2} bonds) and their electrostatic and dispersion effects. Benzene C atom of Ph exhibits sp^2 hybridization, meaning it forms one σ bond and one π bond. The sp^2 hybridization of benzene for Ph explains its limited interaction with TiO_2 clusters and accounts for the substantial adsorption energy. Similar interactions occur with 4-HBA and VL (Fig. S7). Hydrogen bonds form between the H_{-CHO} atom of 4-HBA or VL and the O_{TiO_2} atom, despite the presence of the H_{Ph} atom.

3.3 Continuous-oxidation mechanisms

3.3.1 O_3- and $HO^\bullet$-initiated reactions

PhCs, once released into the atmosphere, undergo several processes, including adsorption on mineral aerosol surfaces, accumulation at the A–W interface, dispersion in bulk water within liquid droplets, and oxidation reactions initiated by atmospheric oxidants (Lin et al., 2017). Reactions inside the aqueous particle have also been a hot topic of interest in recent years (Tilgner et al., 2021; Go et al., 2023; Zhang et al., 2024; Rana et al., 2024), so we also focused on the process by which phenolic compounds enter the interior of the droplet. This section delves into the detailed mechanisms and characteristics of these reactions. At the M06-2X/6-311++G(3df,2p)//M06-2X/6-31+G(d,p) level, the structures with the minimum free energy for Ph, 4-HBA, and VL have been determined (Fig. S10). In the case of VL, a significant reduction in molecular energy is observed due to the formation of a powerful intramolecular hydrogen bond with a length of 2.09 Å between the H and O atoms near the methyl group. Moreover, the lone-pair electrons of oxygen atoms can additionally form p–π conjugations with the π electrons of the phenyl ring, further reducing the overall energy of VL in gas phase. The statistical charts of calculated $\Delta_r G$ and $\Delta G^{\ddagger}$ values for O_3- and $HO^\bullet$-initiated reactions are displayed in Figs. 4 and S8, and further details are available in Tables S1–S4.

O_3 is a major oxidant in the atmosphere, with high concentrations in the troposphere of $9.85 \times 10^{11}\,molec.\,cm^{-3}$ (Tomas et al., 2003; Pillar-Little et al., 2014). Investigating the fate of PhCs in the presence of O_3 is essential (Pillar-Little et al., 2014; Rana and Guzman, 2020). The ozonolysis of PhCs involves the synthesis of primary ozonide, the formation of active Criegee intermediates (CIs), and the disintegration of CIs (Rynjah et al., 2024). The O_3-initiated reactions of Ph, 4-HBA, and VL involve radical adduct formation (RAF) channels on their benzene ring ($R_{O_3-RAF}1$–$R_{O_3-RAF}6$), highlighted in red in Fig. S10. Figure 4a–d show that the ozonolysis pathways R_{O_3-RAF} are exergonic, indicating their spontaneity. The average $\Delta G^{\ddagger}$ values for the ozonolysis of Ph, 4-HBA, and VL are ranked as Ph > VL > 4-HBA. The following is a list of the average values for the ozonolysis of Ph, 4-HBA, and VL, as illustrated in Fig. 4e–h: Ph is superior to VL and 4-HBA, with the exception of TiO_2 clusters. Figure 4e illustrates that the average value of $\Delta G^{\ddagger}$ for $O_3 + Ph$ reactions at the A–W interface is $15.38\,kcal\,mol^{-1}$, the lowest value out of the three PhCs. The average $\Delta G^{\ddagger}$ values for the ozonolysis of Ph, 4-HBA, and VL are as follows: VL ($13.95\,kcal\,mol^{-1}$) < Ph ($24.70\,kcal\,mol^{-1}$) < 4-HBA ($25.16\,kcal\,mol^{-1}$) on TiO_2 clusters (Fig. 4f). The average $\Delta G^{\ddagger}$ values for $O_3 + VL$ reactions in the gas phase are the highest among the four different environmental media ($23.28\,kcal\,mol^{-1}$) shown in Fig. 4g. Comparing the phenolic oxidation in each of these four environmental media (bulk water, interface, TiO_2 clusters, and gas phase) reveals that the A–W interface is more conducive to the ozonolysis of Ph, whereas TiO_2 clusters are more conducive to the ozonolysis of VL. The effect of solvation on $\Delta G^{\ddagger}$ is predominantly caused by the hydration of the phenolic OH group, as this is the part of the molecule being solvated. However, the presence of water molecules in the region around the phenyl group has been shown to have a considerable influence on the $\Delta G^{\ddagger}$ values.

$HO^\bullet$, known as the "atmospheric detergent", is another significant atmospheric oxidant (Atkinson, 1986; Zhang et al., 2020). The worldwide mean tropospheric concentration of $HO^\bullet$ is roughly $11.3 \times 10^5\,molec.\,cm^{-3}$ (Lelieveld et al., 2016). For this reason, elucidating the reaction mechanism underlying $HO^\bullet + PhCs$ reactions in the troposphere is of the utmost importance. $HO^\bullet$-initiated reac-

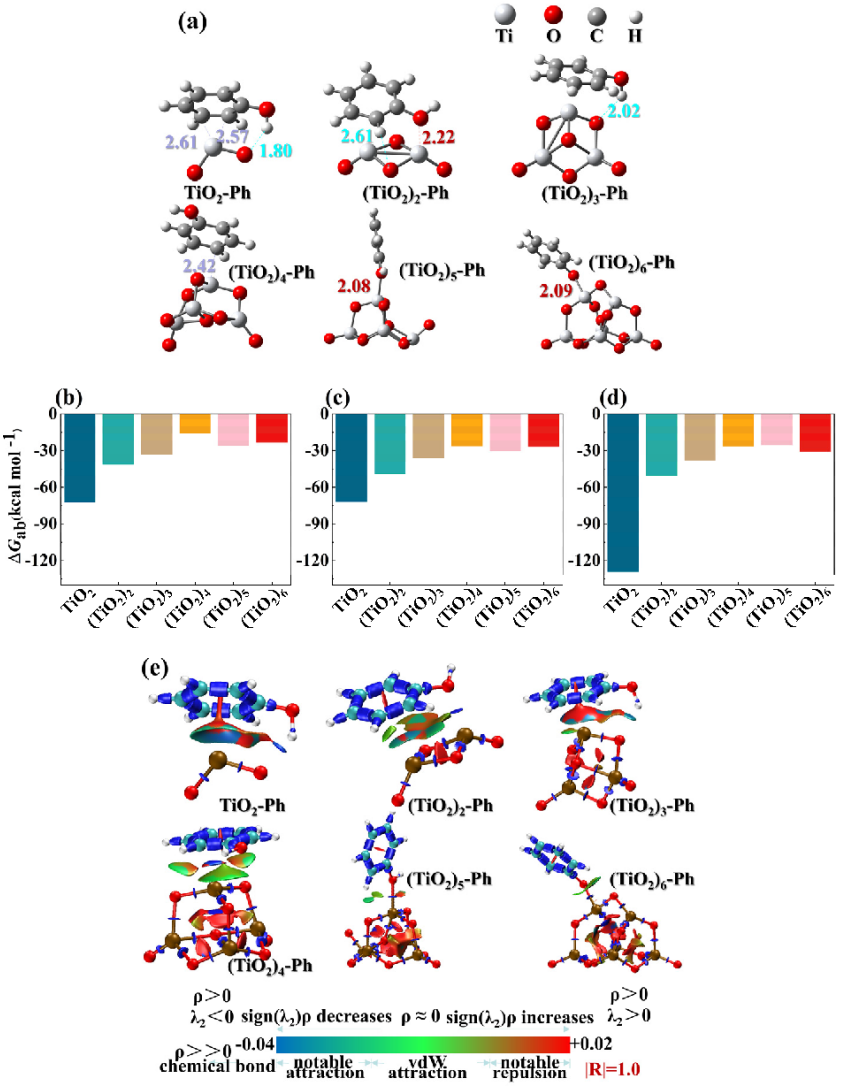

Figure 3. Adsorption details of PhCs on $(TiO_2)_n$ ($n = 1$–6) clusters: **(a)** structure of Ph adsorption on the $(TiO_2)_n$ ($n = 1$–6) surface; adsorption energy of **(b)** Ph, **(c)** 4-HBA, and **(d)** VL on $(TiO_2)_n$ ($n = 1$–6, unit: kcal mol^{-1}); and **(e)** interaction region indicator (IRI) analyses of Ph on the $(TiO_2)_n$ ($n = 1$–6) surface.

tion pathways of Ph, 4-HBA, and VL include RAF, hydrogen atom abstraction (HAA) channels from the benzene ring (R_{HAA}ben1–R_{HAA}ben6), and the substituent group (R_{HAA}sub7–R_{HAA}sub9). Previous research (Gao et al., 2019) has shown that the process of single electron transfer (SET) does not significantly contribute to the HO•-initiated reactions examined. Once the hydroxyl adducts or H_2O are formed, significant heat (4.21–30.28 kcal mol^{-1}) is released (Figs. 4i–l, S8a–d and i–l; detailed data in Table S3), indicating high thermodynamic feasibility. The average $\Delta G^{\ddagger}$ values for HO•-initiated reactions (Figs. 4m–p, S8e–h and m–p) are lower than those for O_3-initiated reactions. Routes R_{HAA}ben make a minimal contribution to HO•-initiated reactions. At the A–W interface, the interaction energies are in the following order: VL (3.52 kcal mol^{-1}) < Ph (4.52 kcal mol^{-1}) < 4-HBA (9.50 kcal mol^{-1}). Additionally, the $\Delta G^{\ddagger}$ value for Ph is the lowest at −0.97 kcal mol^{-1} in the pathways $R_{RAF-HO•}$ (Fig. 4m). Among the three aromatic compounds, the $R_{RAF-HO•}$ routes of VL on TiO_2 clusters are most likely to take place (Fig. 4n). When compared to HO•-initiated reactions of aromatic compounds in the gas phase (Fig. S9e) or bulk water (Fig. S9f), the process of Ph + HO• reactions at the A–W interface is accelerated, whereas the process of VL + HO• reactions is accelerated by TiO_2 clusters. These findings are in agreement with the ozonolysis findings. The same guidelines can be used for routes R_{HAA}sub (Figs. 4o, p and S8g, h) and R_{HAA}ben (Fig. S8m–p). The following is a ranking of the average $\Delta G^{\ddagger}$ values for routes $R_{RAF-HO•}$ in the gas phase or bulk water: Ph < 4-HBA < VL. As a result of having the lowest $\Delta G^{\ddagger}$ values among all HO•-initiated re-

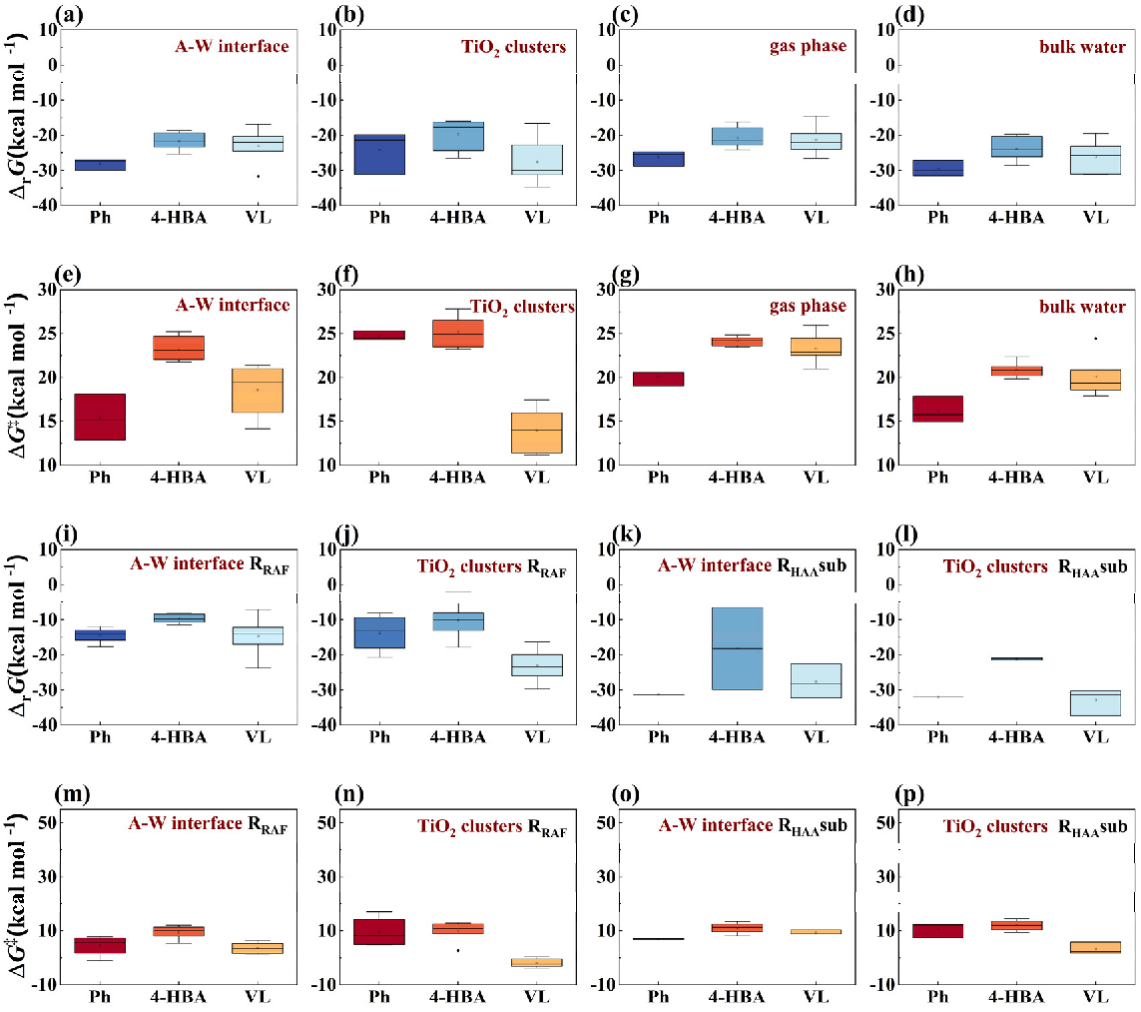

Figure 4. Statistical charts of calculated **(a–d)** $\Delta_r G$ and **(e–h)** $\Delta G^{\ddagger}$ values for O_3-initiated reactions and **(i–l)** $\Delta_r G$ and **(m–p)** $\Delta G^{\ddagger}$ values for HO$^\bullet$-initiated reactions.

action mechanisms, routes R_{RAF} are the most advantageous of all the possible reaction mechanisms. In light of this, each and every route of $R_{RAF-HO\bullet}$ and R_{HAA}sub will be dissected in detail.

Figure 5 shows the $\Delta_r G$ and $\Delta G^{\ddagger}$ values of O_3- and HO$^\bullet$-initiated reactions at various reaction locations. These reactions are almost entirely exothermic, with a close correlation between $\Delta_r G$ values and $\Delta G^{\ddagger}$ values. The $\Delta G^{\ddagger}$ values for the Ph + O_3 reactions shown in Fig. 5a are the lowest among the three compounds, ranging from −0.97 to 7.86 kcal mol^{-1}. Exergonic and spontaneous addition reactions took place at the C1–C2 and C3–C4 locations of Ph and VL, respectively. Because of their low $\Delta G^{\ddagger}$ values, the C1–C2 and C2–C3 sites of O_3-initiated reactions for 4-HBA are advantageous. Their values are 21.76 and 22.03 kcal mol^{-1}, respectively. The C1–C2 location of 4-HBA is activated to a greater extent at the A–W interface in comparison to the gas phase and bulk water. However, the $\Delta G^{\ddagger}$ values of O_3 + Ph reactions on TiO_2 clusters are significantly greater than those of the A–W interface (12.86–18.10 kcal mol^{-1}) at 24.30–25.34 kcal mol^{-1}. The VL + O_3 reactions on TiO_2 clusters are favorable at the C2–C3 and C4–C5 locations (the $\Delta G^{\ddagger}$ values are 11.42 and 11.14 kcal mol^{-1}, respectively, Fig. 5b). This can be explained by the fact that the electron cloud has a greater propensity to congregate in C2–C3 and C4–C5, respectively. In addition, the *p* orbitals of the methoxy and hydroxy groups are conjugated to the benzene ring, which offers a powerful electron-donating conjugation effect (Aracri et al., 2013). Because of this, the oxidation of aromatic molecules is thermodynamically more favorable than the oxidation of the aldehyde group. This is consistent with previous studies that electron density influences the oxidative activity of PhCs (Rana and Guzman, 2022a). Clearly, the $\Delta G^{\ddagger}$ values of HO$^\bullet$-initiated reactions (−0.97 to 13.46 kcal mol^{-1}) in Fig. 5c–f are lower than those of O_3-initiated processes (11.14 to 27.83 kcal mol^{-1}) at different points in the A–W interface and TiO_2 clusters. This can be seen by comparing the values to each other. At the A–W interface, the most

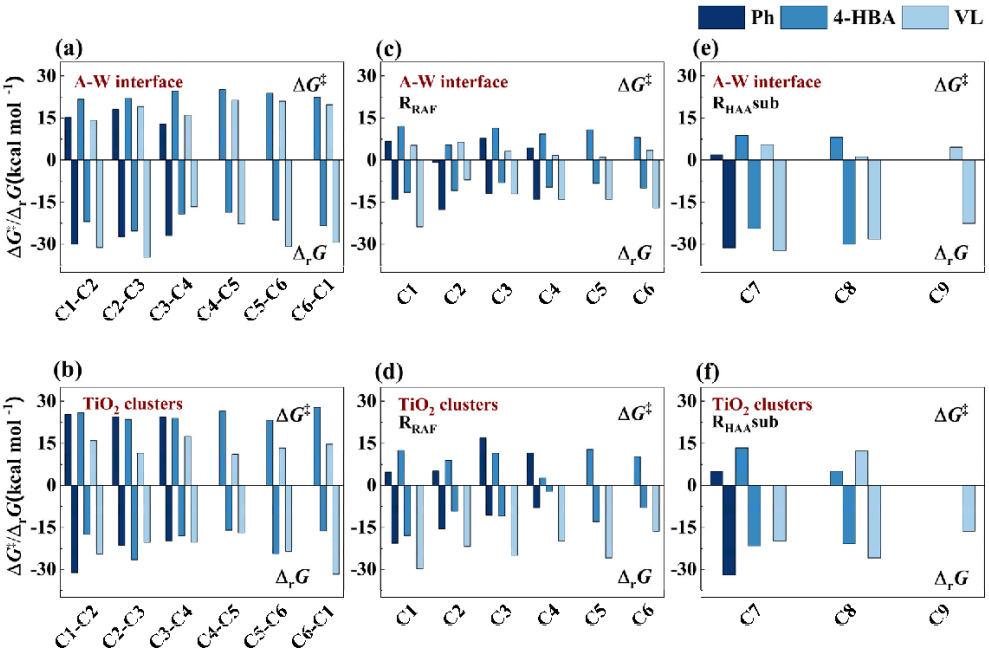

Figure 5. $\Delta_r G$ and $\Delta G^{\ddagger}$ values of **(a–b)** O_3-initiated reactions and **(c–f)** HO•-initiated reactions at different reaction positions.

advantageous position for the phenol hydroxyl group to be in for Ph/4-HBA/VL + HO• reactions is the ortho-position (Fig. 5c). OESI-MS, which stands for online electrospray ionization mass spectrometry, was also able to identify the hydroxylation product known as 3,4-dihydroxybenzaldehyde (Rana and Guzman, 2020). In Fig. 5d, the ortho- and meta-sites of phenol hydroxyl are the most favorable positions for Ph + HO• and 4-HBA + HO• reactions, respectively, on the TiO_2 clusters. On the other hand, all of the VL sites on the TiO_2 clusters are advantageous. At the A–W interface and on the TiO_2 clusters, the abstraction of hydrogen atoms follows the order of H_{-CHO} atom > H_{-OCH_3} atom > H_{-OH} atom in Fig. 5e and f. This can also be explained by the ALIE values of these atoms listed in the same order of H_{-CHO} atom (11.67–11.74 eV) > H_{-OCH_3} atom (14.06 eV) > H_{-OH} atom (15.46 eV), as shown in Fig. S8.

3.3.2 Generation and degradation of key products

For the purposes of this discussion, the primary atmospheric fate of the selected aromatics was considered to be their reactions with O_2 (typically mediated by reactive intermediates or catalytic processes) and O_3. Figures 6 and S10 illustrate the subsequent reaction mechanisms of intermediates (IMs). IM_{1-2} was produced using the pathway that offered the best conditions for the HO•-initiated reaction of Ph. As can be seen in Fig. 6a, the addition of O_2 to the C3 sites of the C_6H_5O radicals results in the formation of C_6H_5O-OO radicals with no barriers in either the gas phase or the bulk water. This is a desirable outcome. For the transformation of the $C_6H_5O_2$-OO radicals that were created, the ring closure reaction to form $C_6H_5O_2$-OO-d is an attractive option. However, it must overcome an energy barrier of 18.83 kcal mol^{-1} in the gas phase or 13.67 kcal mol^{-1} in bulk water. The $C_6H_5O_2$-OO-d_1 radical, which was produced by the $C_6H_5O_2$-OO-d reaction, interacts once more with O_2. In the atmosphere, these Criegee intermediates also may undergo bimolecular reactions with NO_x (Sun et al., 2020). Malealdehyde (P1) is what should mostly result from the reaction of the $C_6H_5O_2$-OO-d_1 radical with NO. However, during this process, it still needs to overcome an energy barrier of 49.5 (in the gas phase) or 50.83 kcal mol^{-1} (in the bulk water) to generate the $C_6H_5O_2$-OO-d_3 radical; as a result, the further transformation of the formed $C_6H_5O_2$-OO-d_2 should continue very slowly. Pyrocatechol (P2) is the primary product generated in the gas phase and bulk water when the H atom of the $C_6H_5O_2$-OO radical is displaced. P2 generates *o*-semiquinone radicals via pathways R_{HAA} by HO• or O_3, which in turn generate oligomers (Guzman et al., 2022). This results in the formation of brown organic carbon in atmospheric aerosols. At the A–W interface, a sequence of hydroxylation products, including pyrocatechol (P2), benzene-1,2,3-triol (P3), and benzene-1,2,3,4,5-pentaol (P4), are generated through hydroxylation processes rather than by a single SET ($\Delta G^{\ddagger} = 111.79$ kcal mol^{-1}). It is difficult for P4 to form benzene-1,2,3,4,5,6-hexaol because it is difficult for hydrogen transfer reactions to occur ($\Delta G^{\ddagger} = 34.32$ kcal mol^{-1}). These hydroxylation products have been detected by experimental means (Pillar-Little et al., 2014; Pillar-Little and Guzman, 2017; Rana and Guzman, 2020). The HO• abstracts a hydrogen atom from the hydroxyl group of catechol, forming a $C_6H_5O_2$ radical and

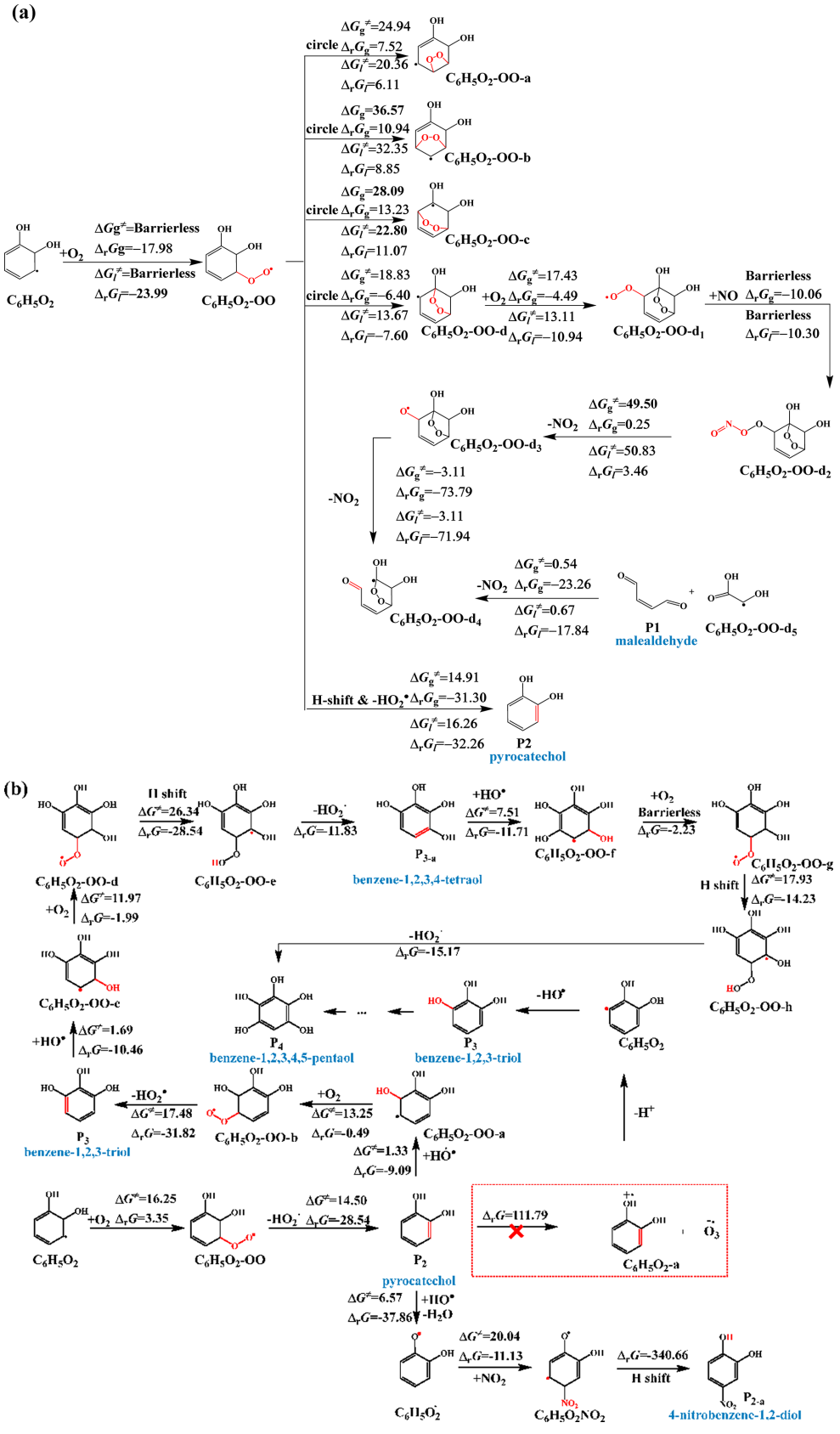

Figure 6. Subsequent reaction mechanisms of important intermediates (IMs) (unit: kcal mol^{-1}) **(a)** in the gas phase (g)/bulk water (l) and **(b)** at the A–W interface.

a water molecule. Due to the widespread presence of NO_2 in the environment, it adds to the $C_6H_5O_2$ radical at the ortho-position of the extracted hydrogen atom through an addition reaction. Subsequently, a hydrogen transfer reaction occurs, resulting in the formation of 4-nitrobenzene-1,2-diol ($P_{2\text{-a}}$). This computational result validates the previous experimental hypothesis by Finewax et al. (2018). The $P_{2\text{-a}}$ subsequently transforms into benzoquinone, maleic acid, fumaric acid, acetic anhydride, acetic acid, and formic acid or is directly mineralized into carbon dioxide and water (Chen et al., 2015). In order to gain a more comprehensive understanding of the reaction mechanism at the A–W interface, the major product (the $C_7H_5O_2$ radical) for pathways R_{HAA} of 4-HBA was also taken into consideration. According to Fig. S11a, the addition of $HO^\bullet$ to the C7 sites of the $C_7H_5O_2$ radical can occur without any obstructions. The overpowering of the 18 kcal mol^{-1} barrier resulted in the formation of the hydroxylation products (4-hydroxybenzoic acid (P5), 3,4-dihydroxybenzoic acid (P6), 2,3,4-trihydroxybenzoic acid (P7), and 2,3,4,5,6-pentahydroxybenzoic acid (P8)). There was found to be one transition route for the continued ozonolysis of the hydroxylation products that were produced in P6. The C2–C3 site of P6 to create P6-5O_3 ($\Delta G^\ddagger = 16.59$ kcal mol^{-1}) has the lowest activation energy of all the available paths for the relevant reactions (Fig. S11b). This corresponds to a value of 16.59 kcal mol^{-1}. When the $\Delta G^\ddagger$ values of the breakage of five-membered rings created by ozonolysis pathways are compared, one can reach the conclusion that the formation of IM_{P6}-5O_3-a is the most favored pathway. All of the hydrogen abstraction processes involving H_2O and IM_{P6}-5O_3-a have rather high energy barriers (32.93 kcal mol^{-1}). On the other hand, in Fig. S10a, the very low $\Delta G^\ddagger$ values (19.74–22.89 kcal mol^{-1}) of the –NO–O abstraction make it a desirable choice. Following a chain of ozonolysis reactions, the following products were obtained (Fig. S11c): ((2*E*,4*Z*)-2-formyl-4,5-dihydroxy-6-oxohexa-2,4-dienoic acid (P9), 2,3-dihydroxymalealdehyde (P10), and 2,3-dioxopropanoic acid (P11). Therefore, the product that was created, P10, may also be the product that was discovered through experimentation (mass-to-charge ratio (m/z) of 115) (Rana and Guzman, 2020). The VL subsequent reaction mechanism is demonstrated in Fig. S11d. The final oxidation products of VL are P12 ((2*E*,4*E*)-4-formyl-2-methoxy-6-oxohexa-2,4-dienoic acid), P13 (ethene-1,1,2-tricarbaldehyde), P14 (2-methoxy-2-oxoacetic acid), P15 (oxalaldehyde), and P16 ((*E*)-2-methoxy-4,5-dioxopent-2-enoic acid). The formation of these products could explain the biomass burning material for the formation of SOA (Rana and Guzman, 2022b).

3.4 Comparison with available experimental results

The rate constants (k) of the overall reaction under the temperature range of 278–318 K were computed based on acquired potential energy surfaces for the O_3-initiated and $HO^\bullet$-initiated reactions of selected compounds. The results of these calculations are listed in Tables S5 and S6, respectively. The temperature dependences of the various k values for Ph, 4-HBA, and VL at the A–W interface and in bulk water are depicted in Fig. 7. At low values of k, there is a positive dependence on temperature. When the k values are raised to a certain degree, the temperature dependency seems to lose any significance it may have had before. The following is an order of the k values for O_3-initiated reactions: A–W_{Ph} > $TiO_{2\,VL}$ > A–W_{VL} > A–$W_{4\text{-HBA}}$ > $TiO_{2\,4\text{-HBA}}$ > $TiO_{2\,Ph}$ (Fig. 7a). According to Fig. 7b, the k values of $HO^\bullet$-initiated reactions are ordered as follows: $TiO_{2\,VL}$ > A–W_{Ph} > A–W_{VL} > $TiO_{2\,4\text{-HBA}}$ > $TiO_{2\,Ph}$ > A–$W_{4\text{-HBA}}$. In Fig. 7a and b, the k values of $HO^\bullet$-initiated reactions are 100 times greater than those of O_3-initiated reactions. Table 1 is a listing of the experimental and estimated k values that are available for O_3-initiated and $HO^\bullet$-initiated reactions at 298 K. According to the findings, the ozonolysis of Ph was promoted by the water–gas interface as well as by TiO_2 clusters, and the $HO^\bullet$-initiated reactions of VL were promoted by TiO_2 clusters. However, the $O_3/HO^\bullet$ + 4-HBA reactions have the lowest k values among the three molecules when tested in a variety of environments. The estimated k_{O_3+Ph} values at the A–W interface are 11 orders of magnitude greater than those of catechol under dry conditions in the gas phase (Zein et al., 2015) when compared with the experimental data. Because it has a higher k_{O_3} value, catechol, which is one of the main products of Ph's oxidation in the atmosphere, has a higher degree of reactivity than its parent compound (Table 1). The estimated value of VL is lower than the experimentally determined value of k_{O_3} for guaiacol under dry conditions, which is $(0.40 \pm 0.31) \times 10^{-18}$ cm^3 molec.$^{-1}$ s^{-1} in the gas phase (Zein et al., 2015). The difference between the predicted value of $k_{HO^\bullet+VL}$ is 1.14×10^{-10} cm^3 molec.$^{-1}$ s^{-1}, and the average experimental value of $k_{HO^\bullet}$ for methoxyphenols is just an order of magnitude. As a consequence, the findings of our calculations are reliable. Previous studies measured the second-order rate constants of guaiacylacetone + $HO^\bullet$ reaction to be $(14–25) \times 10^9$ M^{-1} s^{-1} at pH 5 and 6 for aqueous secondary organic aerosol, which is lower than our results (Arciva et al., 2022). This is because galactose reduces the steady-state concentration of $HO^\bullet$. The reaction rate constants of PhCs increase with increasing pH, and we calculated the rate constants at pH 7 in bulk water (Ma et al., 2021). This study summarizes the O_3- and $HO^\bullet$-initiated reaction sequences of three PhCs in different environmental media. The reaction sequences for O_3- and $HO^\bullet$-initiated reactions of Ph and 4-HBA are identical in different environmental media, while VL shows slight variations. For O_3-initiated reactions, the reaction sequences are as follows: for Ph, A–W interface > bulk water > gas phase > TiO_2 clusters; for 4-HBA, bulk water > A–W interface > TiO_2 clusters > gas phase; and for VL, bulk water > TiO_2 clusters > A–W interface > gas phase. For $HO^\bullet$-initiated reactions,

Table 1. The available experimental and calculated reaction rate constants (k) values of O_3- and HO$^\bullet$-initiated reactions at 298 K. Unit: cm^3 molec.$^{-1}$ s^{-1}.

Compounds	$k_{\text{tot-A–W,cal}}$[a]	$k_{\text{tot-TiO}_2\text{,cal}}$[b]	$k_{\text{tot-gas,cal}}$[c]	$k_{\text{tot-wat,cal}}$[d]	k_{exp}	Ref.
Ph	5.98×10^{-7}	1.84×10^{-24}	5.27×10^{-20}	4.02×10^{12}	$(13.5 \pm 1.1) \times 10^{-18}$[e]	Zein et al. (2015)
	2.69×10^{-6}	3.17×10^{-10}	2.34×10^{-9}	4.46×10^{13}	–	
4-HBA	6.79×10^{-23}	5.32×10^{-24}	4.93×10^{-24}	1.97×10^{12}	–	
	9.49×10^{-11}	3.16×10^{-9}	7.90×10^{-11}	2.52×10^{13}	–	Rana et al. (2024)
VL	1.27×10^{-17}	3.30×10^{-15}	1.35×10^{-22}	2.20×10^{12}	$(0.40 \pm 0.31) \times 10^{-18}$[f]	Zein et al. (2015)
	1.73×10^{-7}	6.70×10^{-6}	1.14×10^{-10}	3.15×10^{13}	6.00×10^{-11}[g]	Rana et al. (2024)

[a] Calculated values of phenolic compounds at A–W interface. [b] Calculated values of phenolic compounds on TiO_2 clusters. [c] Calculated values of phenolic compounds in the gas phase. [d] Calculated values of phenolic compounds in the bulk water. [e] Experimental values of catechol in the gas phase. [f] Experimental values of guaiacol in the gas phase. [g] Experimental average $k_{\text{HO}^\bullet}$ values of methoxyphenols in the gas phase.

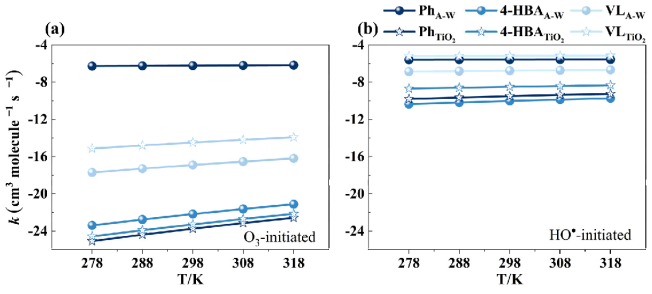

Figure 7. Calculated rate constants for the initial reactions of Ph, 4-HBA, and VL with O_3 and HO$^\bullet$ at different temperatures (278–318 K) and 1 atm.

the sequences are, for Ph, A–W interface ≈ bulk water > gas phase > TiO_2 clusters; for 4-HBA, bulk water > A–W interface > TiO_2 clusters > gas phase; and for VL, TiO_2 clusters > bulk water > A–W interface > gas phase. According to the atmospheric concentration of O_3, the atmospheric lifetime of Ph is the shortest (< 1 s) of the three PhCs at the gas–water interface or in bulk water, whereas 4-HBA and VL were oxidized more slowly than Ph (Smith et al., 2016). See Fig. S12 and Text S9 for ecotoxicity assessment.

4 Conclusions

Combining molecular dynamic simulations (with the AMBER force field) and quantum chemical calculations (at the M06–2X/6–311++G(3df,2p)//M06–2X/6-31+G(d,p) level) methods has provided comprehensive insights into the surface properties of Ph, 4-HBA, and VL, as well as their reactions induced by O_3 and HO$^\bullet$, in both homogenous and heterogenous environments. Here are some key findings from this research:

1. The free-energy well of Ph, 4-HBA, and VL favors the A–W interface as the compounds' preferred location, with occurrence percentages of approximately ∼ 72 %, ∼ 68 %, and ∼ 73 %, respectively. Ph and 4-HBA show a preference for the A–W interface over the air, with an energy difference of around 0.22 and 0.45 kcal mol^{-1}. The VL adsorbed on the TiO_2 clusters has a higher likelihood of remaining compared to VL adsorbed at the A–W interface.

2. The adsorption capacity of TiO_2 clusters decreases with increasing cluster size until $n > 4$. After that point, the adsorption capacity remains constant. Strong electrostatic attractive interactions and attractive dispersion effects occur between the benzene of the Ph and Ti atoms. Hydrogen bonds form between the atom of O_{TiO_2} and the H_{-CHO} group of 4-HBA or VL.

3. The O_3- and HO$^\bullet$-initiated reactions for Ph and VL are facilitated by the A–W interface and TiO_2 clusters, respectively. For O_3-initiated reactions at the A–W interface, the C1–C2 position on the benzene ring is most favorable. Both in the A–W interface and on TiO_2 clusters, the total branching ratio for routes R_{RAF} and R_{HAA}sub is 72.68 %–100 %. For route R_{HAA}sub, the order is H_{-CHO} atom > H_{-OCH_3} atom > H_{-OH} atom.

4. The k values (in molec. cm^{-3} s^{-1}, at 298 K and 1 atm) of O_3-initiated reactions follow the order of A–W_{Ph} (5.98×10^{-7}) > $TiO_{2\,VL}$ (3.30×10^{-15}) > A–W_{VL} (1.27×10^{-17}) > A–$W_{4\text{-HBA}}$ (6.79×10^{-23}) > $TiO_{2\,4\text{-HBA}}$ (5.32×10^{-24}) > $TiO_{2\,Ph}$ (1.84×10^{-24}). The k values of HO$^\bullet$-initiated reactions follow the order of $TiO_{2\,VL}$ (6.70×10^{-6}) > A–W_{Ph} (2.69×10^{-6}) > A–W_{VL} (1.73×10^{-7}) > $TiO_{2\,4\text{-HBA}}$ (3.16×10^{-9}) > $TiO_{2\,Ph}$ (3.17×10^{-10}) > A–$W_{4\text{-HBA}}$ (9.49×10^{-11}).

5. Toxicity risk assessment on aquatic species reveals that most of the reaction products are significantly less harmful than the parent compounds. However, products P1, P2, P3, P10, and P11 are more hazardous, and further investigation of their atmospheric fate is recommended.

Ph undergoes transformation to malealdehyde and catechol when exposed to O_3 or $HO^•$ in the troposphere (Xu and Wang, 2013). When Ph / VL is at the droplet aerosol interface, rapid oxidation to polyhydroxylated compounds occurs (Ma et al., 2021). VL eventually creates tiny molecule aldehydes and acids. This is consistent with experimental observations (Rana and Guzman, 2020). This oxidation process is accelerated when VL is encased in a mineral aerosol represented by TiO_2 clusters. Li et al. (2022) found that seasonal average concentrations of total nitrophenol compounds in particulate matter were comparable to those measured in the gas phase. However, the reactivity order of nitrophenols in the atmospheric compartments is water droplets > gas phase > particles (Vione et al., 2009). The formation of some low-molecular-weight acids and aldehydes (2,3-dihydroxymalealdehyde, 2,3-dioxpropanoic acid, etc.) confirms their association with the formation of SOA. It is recommended that enterprises producing lignin, such as those in the pulp and paper industry, or factories that employ lignin in the manufacturing of adhesives, rust inhibitors, color dispersants, diluents, or other similar products be constructed in regions with low relative humidity. It is recommended that treatment facilities that collect lignin pyrolysis products and recycle the byproducts be located in the surrounding area.

Code availability. The Gaussian 16 software used in this study is a proprietary program developed by Gaussian, Inc. Details about the software can be found at https://gaussian.com (Frisch et al., 2016).

Data availability. The data in this article are available from the corresponding author upon request (hemaox@sdu.edu.cn).

Supplement. The supplement related to this article is available online at: https://doi.org/10.5194/acp-24-12409-2024-supplement.

Author contributions. YH contributed to the manuscript conceptualization, methodology, software, formal analysis, investigation, and writing of the original manuscript. ML provided some ideas for the writing of this paper. XW offered some guidance on the Methods section of the manuscript. JS, YZ, and YM reviewed the original manuscript. MH contributed in terms of conceptualization, resources, writing (review editing), supervision, and funding acquisition.

Competing interests. The contact author has declared that none of the authors has any competing interests.

Disclaimer. Publisher's note: Copernicus Publications remains neutral with regard to jurisdictional claims made in the text, published maps, institutional affiliations, or any other geographical representation in this paper. While Copernicus Publications makes every effort to include appropriate place names, the final responsibility lies with the authors.

Financial support. This research has been supported by the National Natural Science Foundation of China (grant nos. 22276109, 21777087, and 21876099).

Review statement. This paper was edited by Allan Bertram and reviewed by three anonymous referees.

References

Aracri, E., Tzanov, T., and Vidal, T.: Use of Cyclic Voltammetry as an Effective Tool for Selecting Efficient Enhancers for Oxidative Bioprocesses: Importance of pH, Ind. Eng. Chem. Res., 52, 1455–1463, https://doi.org/10.1021/ie3027586, 2013.

Arciva, S., Niedek, C., Mavis, C., Yoon, M., Sanchez, M. E., Zhang, Q., and Anastasio, C.: Aqueous $^•$OH Oxidation of Highly Substituted Phenols as a Source of Secondary Organic Aerosol, Environ. Sci. Technol., 56, 9959–9967, https://doi.org/10.1021/acs.est.2c02225, 2022.

Atkinson, R.: Kinetics and mechanisms of the gas-phase reactions of the hydroxyl radical with organic compounds under atmospheric conditions, Chem. Rev, 86, 69–201, https://doi.org/10.1021/cr00071a004, 1986.

Bai, F.-Y., Ni, S., Ren, Y., Tang, Y.-Z., Zhao, Z., and Pan, X.-M.: DFT analysis on the removal of dimethylbenzoquinones in atmosphere and water environments: $^•$OH-initiated oxidation and captured by $(TiO_2)_n$ clusters ($n = 1$–6), J. Haz. Mat., 386, 121636, https://doi.org/10.1016/j.jhazmat.2019.121636, 2020.

Banerjee, S., Gnanamani, E., Yan, X., and Zare, R. N.: Can all bulk-phase reactions be accelerated in microdroplets?, Analyst, 142, 1399–1402, https://doi.org/10.1039/C6AN02225A, 2017.

Bond, T. C., Streets, D. G., Yarber, K. F., Nelson, S. M., Woo, J.-H., and Klimont, Z.: A technology-based global inventory of black and organic carbon emissions from combustion, J. Geophys. Res.-Atoms., 109, D14203, https://doi.org/10.1029/2003JD003697, 2004.

Cao, H., Wang, K., Yang, Z., Wu, S., and Han, D.: Quantum chemical study on the ozonolysis mechanism of guaiacol and the structure-reactivity relationship of phenols with hydroxyl, methoxy, and methyl substituents, Chem. Eng. J., 420, 127629, https://doi.org/10.1016/j.cej.2020.127629, 2021.

Carena, L., Zoppi, B., Sordello, F., Fabbri, D., Minella, M., and Minero, C.: Phototransformation of Vanillin in Artificial Snow by Direct Photolysis and Mediated by Nitrite, Environ. Sci. Technol., 57, 8785–8795, https://doi.org/10.1021/acs.est.3c01931, 2023.

Chen, C., Chen, H., Yu, J., Han, C., Yan, G., and Guo, S.: p-Nitrophenol Removal by Bauxite Ore Assisted Ozonation and its Catalytic Potential, CLEAN – Soil, Air, Water, 43, 1010–1017, https://doi.org/10.1002/clen.201400330, 2015.

Chen, J., Li, C., Ristovski, Z., Milic, A., Gu, Y., Islam, M. S., Wang, S., Hao, J., Zhang, H., and He, C.: A review of biomass burning: Emissions and impacts on air quality, health

and climate in China, Sci. Total Environ., 579, 1000–1034, https://doi.org/10.1016/j.scitotenv.2016.11.025, 2017.

Chen, P., Li, Y., Zhang, Y., Xue, C., Hopke, P. K., and Li, X.: Dynamic Changes of Composition of Particulate Matter Emissions during Residential Biomass Combustion, Environ. Sci. Technol., 57, 15193–15202, https://doi.org/10.1021/acs.est.3c05412, 2023.

Diehl, B. G., Brown, N. R., Frantz, C. W., Lumadue, M. R., and Cannon, F.: Effects of pyrolysis temperature on the chemical composition of refined softwood and hardwood lignins, Carbon, 60, 531–537, https://doi.org/10.1016/j.carbon.2013.04.087, 2013.

Finewax, Z., de Gouw, J. A., and Ziemann, P. J.: Identification and Quantification of 4-Nitrocatechol Formed from OH and NO_3 Radical-Initiated Reactions of Catechol in Air in the Presence of NO_x: Implications for Secondary Organic Aerosol Formation from Biomass Burning, Environ. Sci. Technol., 52, 1981–1989, https://doi.org/10.1021/acs.est.7b05864, 2018.

Frisch, M. J., Trucks, G. W., Schlegel, H. B., Scuseria, G. E., Robb, M. A., Cheeseman, J. R., Scalmani, G., Barone, V., Petersson, G. A., Nakatsuji, H., Li, X., Caricato, M., Marenich, A. V., Bloino, J., Janesko, B. G., Gomperts, R., Mennucci, B., Hratchian, H. P., Ortiz, J. V., Izmaylov, A. F., Sonnenberg, J. L., Williams, Ding, F., Lipparini, F., Egidi, F., Goings, J., Peng, B., Petrone, A., Henderson, T., Ranasinghe, D., Zakrzewski, V. G., Gao, J., Rega, N., Zheng, G., Liang, W., Hada, M., Ehara, M., Toyota, K., Fukuda, R., Hasegawa, J., Ishida, M., Nakajima, T., Honda, Y., Kitao, O., Nakai, H., Vreven, T., Throssell, K., Montgomery Jr., J. A., Peralta, J. E., Ogliaro, F., Bearpark, M. J., Heyd, J. J., Brothers, E. N., Kudin, K. N., Staroverov, V. N., Keith, T. A., Kobayashi, R., Normand, J., Raghavachari, K., Rendell, A. P., Burant, J. C., Iyengar, S. S., Tomasi, J., Cossi, M., Millam, J. M., Klene, M., Adamo, C., Cammi, R., Ochterski, J. W., Martin, R. L., Morokuma, K., Farkas, O., Foresman, J. B., and Fox, D. J.: Gaussian 16 Rev. C.01, Gaussian, Inc., https://gaussian.com (last access: 5 November 2024), 2016.

Gao, Y., Li, G., Qin, Y., Ji, Y., Mai, B., and An, T.: New theoretical insight into indirect photochemical transformation of fragrance nitro-musks: Mechanisms, ecotoxicity and health effects, Environ. Int., 129, 68–75, https://doi.org/10.1016/j.envint.2019.05.020, 2019.

Go, B. R., Li, Y. J., Huang, D. D., Wang, Y., and Chan, C. K.: Comparison of aqueous secondary organic aerosol (aqSOA) product distributions from guaiacol oxidation by non-phenolic and phenolic methoxybenzaldehydes as photosensitizers in the absence and presence of ammonium nitrate, Atmos. Chem. Phys., 23, 2859–2875, https://doi.org/10.5194/acp-23-2859-2023, 2023.

Grassian, V. H.: New Directions: Nanodust – A source of metals in the atmospheric environment?, Atmos. Environ., 43, 4666–4667, https://doi.org/10.1016/j.atmosenv.2009.06.032, 2009.

Guzman, M. I., Pillar-Little, E. A., and Eugene, A. J.: Interfacial Oxidative Oligomerization of Catechol, ACS Omega, 7, 36009–36016, https://doi.org/10.1021/acsomega.2c05290, 2022.

Hawthorne, S. B., Krieger, M. S., Miller, D. J., and Mathiason, M. B.: Collection and quantitation of methoxylated phenol tracers for atmospheric pollution from residential wood stoves, Environ. Sci. Technol., 23, 470–475, https://doi.org/10.1021/es00181a013, 1989.

Henry, F., Coeur-Tourneur, C., Ledoux, F., Tomas, A., and Menu, D.: Secondary organic aerosol formation from the gas phase reaction of hydroxyl radicals with m-, o- and p-cresol, Atmos. Environ., 42, 3035–3045, https://doi.org/10.1016/j.atmosenv.2007.12.043, 2008.

Hub, J. S., de Groot, B. L., and van der Spoel, D.: g_wham – A Free Weighted Histogram Analysis Implementation Including Robust Error and Autocorrelation Estimates, J. Chem. Theory Comput., 6, 3713–3720, https://doi.org/10.1021/ct100494z, 2010.

Humphrey, W., Dalke, A., and Schulten, K.: VMD: Visual molecular dynamics, J. Mol. Graph. Model., 14, 33–38, https://doi.org/10.1016/0263-7855(96)00018-5, 1996.

Ito, A. and Penner, J. E.: Historical emissions of carbonaceous aerosols from biomass and fossil fuel burning for the period 1870–2000, Global Biogeochem. Cy., 19, GB2028, https://doi.org/10.1029/2004GB002374, 2005.

Jämbeck, J. P. and Lyubartsev, A. P.: Update to the general amber force field for small solutes with an emphasis on free energies of hydration, J. Phys. Chem. B, 118, 3793–3804, https://doi.org/10.1021/jp4111234, 2014.

Jiang, G., Nowakowski, D. J., and Bridgwater, A. V.: Effect of the Temperature on the Composition of Lignin Pyrolysis Products, Energ. Fuel., 24, 4470–4475, https://doi.org/10.1021/ef100363c, 2010.

Jiang, W., Niedek, C., Anastasio, C., and Zhang, Q.: Photoaging of phenolic secondary organic aerosol in the aqueous phase: evolution of chemical and optical properties and effects of oxidants, Atmos. Chem. Phys., 23, 7103–7120, https://doi.org/10.5194/acp-23-7103-2023, 2023.

Kibet, J., Khachatryan, L., and Dellinger, B.: Molecular Products and Radicals from Pyrolysis of Lignin, Environ. Sci. Technol., 46, 12994–13001, https://doi.org/10.1021/es302942c, 2012.

Kroflič, A., Hu, M., Grilc, M., and Grgić, I.: Underappreciated and Complex Role of Nitrous Acid in Aromatic Nitration under Mild Environmental Conditions: The Case of Activated Methoxyphenols, Environ. Sci. Technol., 52, 13756–13765, https://doi.org/10.1021/acs.est.8b01903, 2018.

Kumar, S., Rosenberg, J. M., Bouzida, D., Swendsen, R. H., and Kollman, P. A.: THE weighted histogram analysis method for free-energy calculations on biomolecules. I. The method, J. Comput. Chem., 13, 1011–1021, https://doi.org/10.1002/jcc.540130812, 1992.

Kusaka, R., Nihonyanagi, S., and Tahara, T.: The photochemical reaction of phenol becomes ultrafast at the air–water interface, Nat. Chem., 13, 306–311, https://doi.org/10.1038/s41557-020-00619-5, 2021.

Lee, J. K., Banerjee, S., Nam, H. G., and Zare, R. N.: Acceleration of reaction in charged microdroplets, Q. Rev. Biophys., 48, 437–444, https://doi.org/10.1017/S0033583515000086, 2015a.

Lee, J. K., Kim, S., Nam, H. G., and Zare, R. N.: Microdroplet fusion mass spectrometry for fast reaction kinetics, P. Natl. Acad. Sci. USA, 112, 3898–3903, https://doi.org/10.1073/pnas.1503689112, 2015b.

Lelieveld, J., Gromov, S., Pozzer, A., and Taraborrelli, D.: Global tropospheric hydroxyl distribution, budget and reactivity, Atmos. Chem. Phys., 16, 12477–12493, https://doi.org/10.5194/acp-16-12477-2016, 2016.

Li, M., Wang, X., Zhao, Y., Du, P., Li, H., Li, J., Shen, H., Liu, Z., Jiang, Y., Chen, J., Bi, Y., Zhao, Y., Xue, L., Wang, Y., Chen,

J., and Wang, W.: Atmospheric Nitrated Phenolic Compounds in Particle, Gaseous, and Aqueous Phases During Cloud Events at a Mountain Site in North China: Distribution Characteristics and Aqueous-Phase Formation, J. Geophys. Res.-Atoms., 127, e2022JD037130, https://doi.org/10.1029/2022JD037130, 2022.

Liao, Y., Koelewijn, S.-F., Van den Bossche, G., Van Aelst, J., Van den Bosch, S., Renders, T., Navare, K., Nicolaï, T., Van Aelst, K., Maesen, M., Matsushima, H., Thevelein, J. M., Van Acker, K., Lagrain, B., Verboekend, D., and Sels, B. F.: A Sustainable Wood Biorefinery for Low-Carbon Footprint Chemicals Production, Science, 367, 1385–1390, https://doi.org/10.1126/science.aau1567, 2020.

Lin, P.-C., Wu, Z.-H., Chen, M.-S., Li, Y.-L., Chen, W.-R., Huang, T.-P., Lee, Y.-Y., and Wang, C. C.: Interfacial Solvation and Surface pH of Phenol and Dihydroxybenzene Aqueous Nanoaerosols Unveiled by Aerosol VUV Photoelectron Spectroscopy, J. Phys. Chem. B, 121, 1054–1067, https://doi.org/10.1021/acs.jpcb.6b10201, 2017.

Liu, C., Liu, J., Liu, Y., Chen, T., and He, H. J. A. E.: Secondary organic aerosol formation from the OH-initiated oxidation of guaiacol under different experimental conditions, Atmos. Environ., 207, 30–37, https://doi.org/10.1016/j.atmosenv.2019.03.021, 2019.

Liu, C., Chen, D., and Chen, X. E.: Atmospheric Reactivity of Methoxyphenols: A Review, Environ. Sci. Technol., 56, 2897–2916, https://doi.org/10.1021/acs.est.1c06535, 2022.

Lou, R., Wu, S.-B., and Lv, G.-J.: Effect of conditions on fast pyrolysis of bamboo lignin, J. Anal. Appl. Pyrol., 89, 191–196, https://doi.org/10.1016/j.jaap.2010.08.007, 2010.

Lu, T. and Chen, F.: Multiwfn: A multifunctional wavefunction analyzer, J. Comput. Chem., 33, 580–592, https://doi.org/10.1002/jcc.22885, 2012.

Lu, T. and Chen, Q.: Interaction Region Indicator: A Simple Real Space Function Clearly Revealing Both Chemical Bonds and Weak Interactions, Chemistry–Methods, 1, 231–239, https://doi.org/10.1002/cmtd.202100007, 2021.

Ma, L., Guzman, C., Niedek, C., Tran, T., Zhang, Q., and Anastasio, C.: Kinetics and Mass Yields of Aqueous Secondary Organic Aerosol from Highly Substituted Phenols Reacting with a Triplet Excited State, Environ. Sci. Technol., 55, 5772–5781, https://doi.org/10.1021/acs.est.1c00575, 2021.

Nollet, H., Roels, M., Lutgen, P., Van der Meeren, P., and Verstraete, W.: Removal of PCBs from wastewater using fly ash, Chemosphere, 53, 655–665, https://doi.org/10.1016/S0045-6535(03)00517-4, 2003.

Pillar-Little, E. A. and Guzman, M. I.: Oxidation of Substituted Catechols at the Air–Water Interface: Production of Carboxylic Acids, Quinones, and Polyphenols, Environ. Sci. Technol., 51, 4951–4959, https://doi.org/10.1021/acs.est.7b00232, 2017.

Pillar-Little, E. A., Camm, R. C., and Guzman, M. I.: Catechol Oxidation by Ozone and Hydroxyl Radicals at the Air–Water Interface, Environ. Sci. Technol., 48, 14352–14360, https://doi.org/10.1021/es504094x, 2014.

Qu, Z.-W. and Kroes, G.-J.: Theoretical Study of the Electronic Structure and Stability of Titanium Dioxide Clusters $(TiO_2)_n$ with $n = 1$–9, J. Phys. Chem. B, 110, 8998–9007, https://doi.org/10.1021/jp056607p, 2006.

Rana, M. S. and Guzman, M. I.: Oxidation of Phenolic Aldehydes by Ozone and Hydroxyl Radicals at the Air–Water Interface, J. Phys. Chem. A, 124, 8822–8833, https://doi.org/10.1021/acs.jpca.0c05944, 2020.

Rana, M. S. and Guzman, M. I.: Oxidation of Phenolic Aldehydes by Ozone and Hydroxyl Radicals at the Air–Solid Interface, Acs Earth Space Chem., 6, 2900–2909, https://doi.org/10.1021/acsearthspacechem.2c00206, 2022a.

Rana, M. S. and Guzman, M. I.: Surface Oxidation of Phenolic Aldehydes: Fragmentation, Functionalization, and Coupling Reactions, J. Phys. Chem. A, 126, 6502–6516, https://doi.org/10.1021/acs.jpca.2c04963, 2022b.

Rana, M. S. and Guzman, M. I.: Oxidation of Catechols at the Air–Water Interface by Nitrate Radicals, Environ. Sci. Technol., 56, 15437–15448, https://doi.org/10.1021/acs.est.2c05640, 2022c.

Rana, M. S., Bradley, S. T., and Guzman, M. I.: Conversion of Catechol to 4-Nitrocatechol in Aqueous Microdroplets Exposed to O_3 and NO_2, ACS ES&T Air, 1, 80–91, https://doi.org/10.1021/acsestair.3c00001, 2024.

Reid, J. S., Eck, T. F., Christopher, S. A., Koppmann, R., Dubovik, O., Eleuterio, D. P., Holben, B. N., Reid, E. A., and Zhang, J.: A review of biomass burning emissions part III: intensive optical properties of biomass burning particles, Atmos. Chem. Phys., 5, 827–849, https://doi.org/10.5194/acp-5-827-2005, 2005.

Roeselová, M., Vieceli, J., Dang, L. X., Garrett, B. C., and Tobias, D. J.: Hydroxyl Radical at the Air-Water Interface, J. Am. Chem. Soc., 126, 16308–16309, https://doi.org/10.1021/ja045552m, 2004.

Rogge, W. F., Hildemann, L. M., Mazurek, M. A., and Cass, G. R.: Sources of Fine Organic Aerosol. 9. Pine, Oak, and Synthetic Log Combustion in Residential Fireplaces, Environ. Sci. Technol., 32, 13–22, https://doi.org/10.1021/es960930b, 1998.

Rubasinghege, G., Elzey, S., Baltrusaitis, J., Jayaweera, P. M., and Grassian, V. H.: Reactions on Atmospheric Dust Particles: Surface Photochemistry and Size-Dependent Nanoscale Redox Chemistry, J. Phys. Chem. Lett., 1, 1729–1737, https://doi.org/10.1021/jz100371d, 2010.

Rynjah, S., Baro, B., and Sarkar, B.: Oxepin Derivatives Formation from Gas-Phase Catechol Ozonolysis, J. Phys. Chem. A, 128, 251–260, https://doi.org/10.1021/acs.jpca.3c04582, 2024.

Sakata, K., Takahashi, Y., Takano, S., Matsuki, A., Sakaguchi, A., and Tanimoto, H.: First X-ray Spectroscopic Observations of Atmospheric Titanium Species: Size Dependence and the Emission Source, Environ. Sci. Technol., 55, 10975–10986, https://doi.org/10.1021/acs.est.1c02000, 2021.

Shang, H., Wang, X., Li, H., Li, M., Mao, C., Xing, P., Zhao, S., Chen, Z., Sun, J., Ai, Z., and Zhang, L.: Oxygen vacancies promote sulfur species accumulation on TiO_2 mineral particles, Appl. Catal. B Environ., 290, 120024, https://doi.org/10.1016/j.apcatb.2021.120024, 2021.

Shi, Q., Zhang, W., Ji, Y., Wang, J., Qin, D., Chen, J., Gao, Y., Li, G., and An, T.: Enhanced uptake of glyoxal at the acidic nanoparticle interface: implications for secondary organic aerosol formation, Environ. Sci.-Nano, 7, 1126–1135, https://doi.org/10.1039/D0EN00016G, 2020.

Simoneit, B. R. T.: Biomass burning – a review of organic tracers for smoke from incomplete combustion, Appl. Geochem., 17, 129–162, https://doi.org/10.1016/S0883-2927(01)00061-0, 2002.

Smith, J. D., Kinney, H., and Anastasio, C.: Phenolic carbonyls undergo rapid aqueous photodegradation to form low-

volatility, light-absorbing products, Atmos. Environ., 126, 36–44, https://doi.org/10.1016/j.atmosenv.2015.11.035, 2016.

Soongprasit, K., Sricharoenchaikul, V., and Atong, D.: Phenol-derived products from fast pyrolysis of organosolv lignin, Energy Rep., 6, 151–167, https://doi.org/10.1016/j.egyr.2020.08.040, 2020.

Sun, J., Han, D., Shallcross, D. E., Cao, H., Wei, B., Mei, Q., Xie, J., Zhan, J., and He, M.: Theoretical studies on the heterogeneous ozonolysis of syringol on graphene: Mechanism, kinetics and ecotoxicity assessment, Chem. Eng. J., 404, 126484, https://doi.org/10.1016/j.cej.2020.126484, 2021.

Sun, N., Rodríguez, H., Rahman, M., and Rogers, R. D.: Where are ionic liquid strategies most suited in the pursuit of chemicals and energy from lignocellulosic biomass?, Chem. Commun., 47, 1405–1421, https://doi.org/10.1039/C0CC03990J, 2011.

Sun, Y., Chen, X., Xu, F., and Wang, X.: Quantum chemical calculations on the mechanism and kinetics of ozone-initiated removal of p-coumaryl alcohol in the atmosphere, Chemosphere, 253, 126744, https://doi.org/10.1016/j.chemosphere.2020.126744, 2020.

Sun, Y., Chen, X., Liu, L., Xu, F., and Zhang, X.: Mechanisms and kinetics studies of the atmospheric oxidation of eugenol by hydroxyl radicals and ozone molecules, Sci. Total Environ., 770, 145203, https://doi.org/10.1016/j.scitotenv.2021.145203, 2021.

Tilgner, A., Schaefer, T., Alexander, B., Barth, M., Collett Jr., J. L., Fahey, K. M., Nenes, A., Pye, H. O. T., Herrmann, H., and McNeill, V. F.: Acidity and the multiphase chemistry of atmospheric aqueous particles and clouds, Atmos. Chem. Phys., 21, 13483–13536, https://doi.org/10.5194/acp-21-13483-2021, 2021.

Tomas, A., Olariu, R. I., Barnes, I., and Becker, K. H.: Kinetics of the reaction of O_3 with selected benzenediols, Int. J. Chem. Kinet., 35, 223–230, https://doi.org/10.1002/kin.10121, 2003.

Vione, D., Maurino, V., Minero, C., Duncianu, M., Olariu, R.-I., Arsene, C., Sarakha, M., and Mailhot, G.: Assessing the transformation kinetics of 2- and 4-nitrophenol in the atmospheric aqueous phase. Implications for the distribution of both nitroisomers in the atmosphere, Atmos. Environ., 43, 2321–2327, https://doi.org/10.1016/j.atmosenv.2009.01.025, 2009.

Wang, R., Li, K., Li, J., Tsona, N. T., Wang, W., and Du, L.: Interaction of Acrylic Acid and SO_2 on the Surface of Mineral Dust Aerosol, Acs Earth Space Chem., 7, 548–558, https://doi.org/10.1021/acsearthspacechem.2c00323, 2023.

Xu, C. and Wang, L.: Atmospheric Oxidation Mechanism of Phenol Initiated by OH Radical, J. Phys. Chem. A, 117, 2358–2364, https://doi.org/10.1021/jp308856b, 2013.

Yan, X., Bain, R. M., and Cooks, R. G.: Organic Reactions in Microdroplets: Reaction Acceleration Revealed by Mass Spectrometry, Angew. Chem. Int. Ed., 55, 12960–12972, https://doi.org/10.1002/anie.201602270, 2016.

Yao, L., Yang, L., Chen, J., Wang, X., Xue, L., Li, W., Sui, X., Wen, L., Chi, J., Zhu, Y., Zhang, J., Xu, C., Zhu, T., and Wang, W.: Characteristics of carbonaceous aerosols: Impact of biomass burning and secondary formation in summertime in a rural area of the North China Plain, Sci. Total Environ., 557–558, 520–530, https://doi.org/10.1016/j.scitotenv.2016.03.111, 2016.

Yee, L. D., Kautzman, K. E., Loza, C. L., Schilling, K. A., Coggon, M. M., Chhabra, P. S., Chan, M. N., Chan, A. W. H., Hersey, S. P., Crounse, J. D., Wennberg, P. O., Flagan, R. C., and Seinfeld, J. H.: Secondary organic aerosol formation from biomass burning intermediates: phenol and methoxyphenols, Atmos. Chem. Phys., 13, 8019–8043, https://doi.org/10.5194/acp-13-8019-2013, 2013.

Yuan, S., Wang, X., Jiang, Z., Zhang, H., and Yuan, S.: Contribution of air-water interface in removing PFAS from drinking water: Adsorption, stability, interaction and machine learning studies, Water Res., 236, 119947, https://doi.org/10.1016/j.watres.2023.119947, 2023.

Zein, A. E., Coeur, C., Obeid, E., Lauraguais, A., and Fagniez, T.: Reaction Kinetics of Catechol (1,2-Benzenediol) and Guaiacol (2-Methoxyphenol) with Ozone, J. Phys. Chem. A, 119, 6759–6765, https://doi.org/10.1021/acs.jpca.5b00174, 2015.

Zhang, J., Shrivastava, M., Ma, L., Jiang, W., Anastasio, C., Zhang, Q., and Zelenyuk, A.: Modeling Novel Aqueous Particle and Cloud Chemistry Processes of Biomass Burning Phenols and Their Potential to Form Secondary Organic Aerosols, Environ. Sci. Technol., 58, 3776–3786, https://doi.org/10.1021/acs.est.3c07762, 2024.

Zhang, W., Ji, Y., Li, G., Shi, Q., and An, T.: The heterogeneous reaction of dimethylamine/ammonia with sulfuric acid to promote the growth of atmospheric nanoparticles, Environ. Sci.-Nano, 6, 2767–2776, https://doi.org/10.1039/C9EN00619B, 2019.

Zhang, W., Tong, S., Jia, C., Wang, L., Liu, B., Tang, G., Ji, D., Hu, B., Liu, Z., Li, W., Wang, Z., Liu, Y., Wang, Y., and Ge, M.: Different HONO Sources for Three Layers at the Urban Area of Beijing, Environ. Sci. Technol., 54, 12870–12880, https://doi.org/10.1021/acs.est.0c02146, 2020.

Zhong, J., Kumar, M., Anglada, J. M., Martins-Costa, M. T. C., Ruiz-Lopez, M. F., Zeng, X. C., and Francisco, J. S.: Atmospheric Spectroscopy and Photochemistry at Environmental Water Interfaces, Annu. Rev. Phys. Chem., 70, 45–69, https://doi.org/10.1146/annurev-physchem-042018-052311, 2019.